

Numerical Analysis on Standing Accretion Shock Instability with Neutrino Heating in the Supernova Cores

Naofumi Ohnishi¹, Kei Kotake², and Shoichi Yamada^{2,3}

¹*Department of Aerospace Engineering, Tohoku University, 6-6-01 Aramaki-Aza-Aoba, Aoba-ku, Sendai, 980-8579, Japan*

ohnishi@cfm.mech.tohoku.ac.jp

²*Science & Engineering, Waseda University, 3-4-1 Okubo, Shinjuku, Tokyo, 169-8555, Japan*

kkotake@heap.phys.waseda.ac.jp

³*Advanced Research Institute for Science and Engineering, Waseda University, 3-4-1 Okubo, Shinjuku, Tokyo, 169-8555, Japan*

shoichi@waseda.jp

ABSTRACT

We have numerically studied the instability of the spherically symmetric standing accretion shock wave against non-spherical perturbations. We have in mind the application to the collapse-driven supernovae in the post bounce phase, where the prompt shock wave generated by core bounce is commonly stalled. We take an experimental stand point in this paper. Using spherically symmetric, completely steady, shocked accretion flows as unperturbed states, we have clearly observed both the linear growth and the subsequent nonlinear saturation of the instability. In so doing, we have employed a realistic equation of state together with heating and cooling via neutrino reactions with nucleons. We have done a mode analysis based on the spherical harmonics decomposition and found that the modes with $\ell = 1, 2$ are dominant not only in the linear regime, but also after the nonlinear couplings generate various modes and the saturation occurs. Varying the neutrino luminosity, we have constructed the unperturbed states both with and without a negative entropy-gradient. We have found that in both cases the growth of the instability is similar, suggesting the convection does not play a dominant role, which also appears to be supported by the recent linear analysis of the convection in accretion flows by Foglizzo et al. The real part of the eigen frequency seems to be mainly determined by the advection time rather than by the sound-crossing time. Whatever the cause may be, the instability is favorable for the shock revival.

Subject headings: supernovae: collapse — neutrinos — hydrodynamics — instability

1. Introduction

Over the last decades, it has been observationally suggested that the core-collapse supernovae are generally aspherical (Wang et al. 1996, 2001, 2002). The most unequivocal example is SN1987A. Recent HST images of SN1987A are directly showing that the expanding envelope is indeed elliptical with the long axis aligned with the rotation axis inferred from the ring. The aspect ratio and the position angle of the symmetry axis are consistent with those predicted earlier from the observations of speckle and linear polarization. What is more, the linear polarization became greater as the time passed (Wang et al. 2001; Leonard et al. 2001), the fact which has been used to argue that the central engine of the explosion is responsible for the non-sphericity (Khokhlov et al. 1999; Wheeler et al. 2000). Rather common detections of the linear polarization in other core-collapse supernovae seem to suggest, as mentioned at the beginning, that the core-collapse supernovae are globally asymmetric in general.

Various physical ingredients have been proposed as a possible cause of the asymmetry so far: convections below the shock wave as well as inside the proto neutron star (Herant et al. (1994); Burrows et al. (1995); Janka & Mueller (1996), see for a review Janka et al. (2001)), density inhomogeneities produced prior to core-collapse (Burrows & Hayes 1996; Fryer 2004), rapid rotation of the core (Mönchmeyer & Müller 1989; Yamada & Sato 1994; Shimizu et al. 2001; Kotake et al. 2003; Yamasaki & Yamada 2005; Walder et al. 2005), and magnetic fields (Ardeljan et al. 2000; Akiyama et al. 2003; Kotake et al. 2004; Yamada & Sawai 2004; Kotake et al. 2005) (see for a review, Kotake et al. (2005) and references therein). These studies have also been motivated by the interest in the consequences of the asymmetric motions to the explosion mechanism itself, since it has been expected that the deviation from the spherical symmetry will be helpful for the shock revival one way or another.

Recently, Blondin et al. (2003) demonstrated numerically that yet another hydrodynamical mechanism may be conspiring to drive non-spherical motions in the flow below the shock wave. The so-called standing accretion shock instability (SASI) is supposed to be a non-local hydrodynamical instability possibly caused by the cycle of the inward advection of velocity- and entropy-perturbations and outward propagation of acoustic waves, with fluctuations amplified after each cycle. This mechanism of SASI was originally studied in linear analysis by Foglizzo (2001, 2002) in the context of accreting black holes (see also Houck &

Chevalier (1992)). Adding small non-spherical perturbations to the spherically symmetric, isentropic, steady, post-shock accretion flows, Blondin et al. (2003) found in their numerical simulations that the perturbations grow up to the nonlinear regime with clear dominance of $\ell = 1$ at first and $\ell = 2$ later, leading to the global deformation of the shock wave. Here ℓ stands for the azimuthal index of the Legendre polynomials. One lesson to learn is that we should not impose the symmetry with respect to the equatorial plane in the simulations.

As mentioned already, since the large deviation from the spherical symmetry may have an important consequence to the explosion itself, the finding of Blondin et al. (2003) has much interest of other researchers. In their first paper (Blondin et al. 2003), the neutrino heating and cooling are entirely ignored and the flow is assumed to be isentropic. In the recent paper (Blondin & Mezzacappa 2005), the authors took into account the cooling term of a simple analytic form just as in Houck & Chevalier (1992), but no heating included yet. On the other hand, Scheck et al. (2004) demonstrated that similar asymmetric motions with no equatorial symmetry occur in their most realistic numerical models. Although their results show that the neutrino processes will not nullify SASI, the growths and saturations of individual modes under neutrino-irradiation are not clear, since they used highly complicated flows as an underlying model.

Our standing point in this paper is somewhere in between these works. We study SASI by 2D axisymmetric hydrodynamical simulations. Although we have in mind the application to the supernova core in the shock-stagnation phase, we take an experimental stance as in Blondin et al. (2003). On the one hand, we employ a realistic equation of state (Shen et al. 1998) and take into account the heating and cooling of matter via neutrino emissions and absorptions on nucleons. As an underlying model, on the other hand, we utilize the spherically symmetric, steady, shocked accretion flows (Yamasaki & Yamada 2005), which is stable against radial perturbations. Although this is certainly a crude approximation to what we found in the realistic simulations, it will enable us to do clear mode-analyses from the linear growths through the nonlinear couplings among various modes up to the eventual saturation of SASI. Due to the neutrino-heating, some initial models have a convectively unstable region in the classical sense (see Foglizzo et al. (2005)) and SASI is inevitably mixed with convection. By lowering the neutrino luminosity, however, we can also construct models with no convectively unstable region. By comparing these models, we can assess the relative strength of these instabilities. We also discuss the implications that SASI might have for the shock revival.

The plan of this paper is as follows. We describe the numerical methods in section 2. The main numerical results are shown in section 3. We conclude this paper in section 4.

2. Numerical Methods and Models

2.1. Basic Equations

Assuming the axisymmetry of the system in this paper, we numerically study the growth of the non-spherical instability in the accretion flow through the shock wave onto the proton-neutron star. The unperturbed steady accretion flows and the shock waves are assumed to be spherically symmetric. We take into account the heating and cooling of accreting matter via neutrino absorptions and emissions by free nucleons. Only the region outside the neutrino sphere is considered.

The basic evolution equations are written as follows,

$$\frac{d\rho}{dt} + \rho \nabla \cdot \mathbf{v} = 0, \quad (1)$$

$$\rho \frac{d\mathbf{v}}{dt} = -\nabla P - \rho \nabla \Phi, \quad (2)$$

$$\rho \frac{d}{dt} \left(\frac{e}{\rho} \right) = -P \nabla \cdot \mathbf{v} + Q_E, \quad (3)$$

$$\frac{dY_e}{dt} = Q_N, \quad (4)$$

$$\Phi = -\frac{GM_{\text{in}}}{r}, \quad (5)$$

where $\rho, \mathbf{v}, e, P, Y_e, \Phi$ are density, velocity, internal energy, pressure, electron fraction, and gravitational potential of the central object, respectively. The self-gravity of matter in the accretion flow is ignored. Q_E and Q_N are related with the interactions with neutrinos and are explained in more detail in the next section. We denote the Lagrangian derivative as d/dt and r is the radius.

The numerical code for hydrodynamic computations employed in this paper is based on the ZEUS-2D (Stone & Norman 1992), which is an Eulerian code based on the finite-difference method and employs an artificial viscosity of von Neumann and Richtmyer type to capture shocks. We have made several major changes to the base code to include the microphysics as described in the following sections. First, we have added the equation for electron fraction (Eq. (4)), which is solved in the operator-splitting fashion. Second, we have incorporated the tabulated realistic equation of state (EOS) based on the relativistic mean field theory (Shen et al. 1998) instead of the ideal gas EOS assumed in the original code.

Spherical coordinates are used. No equatorial symmetry is assumed and the computation domain covers the whole meridian section with 60 angular mesh points, except for a model

in which we adopted 120 angular grid points. Since the latter model did not produce any significant difference from other models, we will report in the following the results obtained from the models with 60 angular mesh points. We use 300 radial mesh points to cover $r_{\text{in}} \leq r \leq r_{\text{out}} = 2000$ km, where r_{in} is the inner boundary and chosen to be the radius of neutrino sphere, r_ν , defined later.

2.2. Neutrino Absorptions and Emissions by Free Nucleons

Q_E and Q_N in Eqs. (3) and (4) are concerning the absorptions and emissions of electron-type neutrino ν_e and anti-neutrino $\bar{\nu}_e$ on free nucleons. We summarize here the expressions for these terms together with the approximations we employ in this paper.

The neutrino absorptivity on free neutron ($\nu_e + n \rightarrow e^- + p$) is written as follows (Bruenn 1985; Rampp & Janka 2002),

$$\kappa(\epsilon) = \mathcal{G}\eta_{\text{np}}(3g_A^2 + g_V^2) [1 - F_e(\epsilon + \Delta)] (\epsilon + \Delta) \sqrt{(\epsilon + \Delta)^2 - m_e^2 c^4}, \quad (6)$$

where m_e , c , ϵ are electron mass, speed of light, and neutrino energy, respectively. \mathcal{G} is defined as follows,

$$\mathcal{G} = \frac{\sigma_0}{4m_e^2 c^4}, \quad (7)$$

where the characteristic cross section of weak interaction, σ_0 , is given as

$$\sigma_0 = \frac{4(m_e c^2 G_F)^2}{\pi(\hbar c)^4} = 1.761 \cdot 10^{-44} \text{ cm}^2. \quad (8)$$

In the above equation, G_F is the Fermi constant. Δ is the difference of rest mass energies of neutron and proton;

$$\Delta = m_n c^2 - m_p c^2. \quad (9)$$

The nucleon form factors for the vector and axial vector currents are set to be $g_V = 1$ and $g_A = 1.23$, respectively. The degeneracy factor, η_{np} , is defined by

$$\eta_{\text{np}} = 2 \int \frac{d^3 p}{(2\pi\hbar c)^3} F_n(\epsilon) [1 - F_p(\epsilon)]. \quad (10)$$

F_i is the Fermi-Dirac distribution function for species i ;

$$F_i(\epsilon_i) = 1 / [1 + \exp((\epsilon_i - \mu_i) / k_B T)], \quad (11)$$

where k_B , T , μ_i are Boltzmann constant, temperature, and chemical potential including rest mass, respectively. The emissivity of ν_e can be obtained from the absorptivity by detailed balance as

$$j(\epsilon) = \exp[-(\epsilon - (\mu_p - \mu_n + \mu_e)) / k_B T] \kappa(\epsilon). \quad (12)$$

The absorptivity of anti-neutrino on free proton ($\bar{\nu}_e + p \rightarrow e^+ + n$) is similarly represented by

$$\kappa(\epsilon) = \mathcal{G}\eta_{\text{pn}}(3g_A^2 + g_V^2) [1 - F_{e^+}(\epsilon - \Delta)] (\epsilon - \Delta) \sqrt{(\epsilon - \Delta)^2 - m_e^2 c^4} \Theta(\epsilon - \Delta - m_e c^2), \quad (13)$$

where $\Theta(\epsilon)$ is the step function;

$$\Theta(\epsilon) = \begin{cases} 1 & \text{for } \epsilon \geq 0 \\ 0 & \text{for } \epsilon < 0 \end{cases}. \quad (14)$$

The degeneracy factor, η_{pn} , is defined by exchanging the contributions from proton and neutron in Eq. (10). The emissivity is obtained again by the detailed balance just like for Eq. (12) together with the relation of $\mu_{e^+} = -\mu_e$;

$$j(\epsilon) = \exp[-(\epsilon - (\mu_n - \mu_p - \mu_e)) / k_B T] \kappa(\epsilon). \quad (15)$$

Using the absorptivities and emissivities given above, Q_E and Q_N can be expressed as follows,

$$Q_E = -\frac{4\pi c}{(2\pi\hbar c)^3} \int_0^\infty \epsilon^3 d\epsilon [j(\epsilon) - (j(\epsilon) + \kappa(\epsilon)) f(r, \epsilon)], \quad (16)$$

$$Q_N = i \frac{m_B}{\rho} \frac{4\pi c}{(2\pi\hbar c)^3} \int_0^\infty \epsilon^2 d\epsilon [j(\epsilon) - (j(\epsilon) + \kappa(\epsilon)) f(r, \epsilon)], \quad (17)$$

$$\begin{cases} i = -1 & \text{(for electron-type neutrino)} \\ i = 1 & \text{(for electron-type antineutrino)} \end{cases},$$

where $f(r, \epsilon)$ is the distribution function of neutrino. These rates are calculated for ν_e and $\bar{\nu}_e$ separately and summed for the source terms in Eqs. (3) and (4).

Since we deal with the optically thin region outside the neutrino sphere in this paper, we do not have to solve the transport equation for neutrinos. We assume that the neutrino distribution functions are approximated by the Fermi-Dirac distribution with a vanishing chemical potential;

$$f(r, \epsilon) = \frac{1}{1 + \exp(\epsilon/k_B T_\nu)} \cdot \frac{1 - \sqrt{1 - (r_\nu/r)^2}}{2\pi}, \quad (18)$$

where the geometrical factor is taken into account for normalization. Note that although the angular dependence in the above distribution function is assumed to be isotropic, it is entirely irrelevant for the absorption and emission rates. We further assume for simplicity in the following that the luminosity L_ν , temperature T_ν and neutrino sphere r_ν are related by the following equation,

$$L_\nu = \frac{7}{16} \sigma T_\nu^4 \cdot 4\pi r_\nu^2, \quad (19)$$

where σ is the Stefan-Boltzmann constant.

2.3. Initial and Boundary Conditions

In order to clearly see the linear growths of the instability, it is critically important to use a well-defined unperturbed state as an initial condition for simulations. For this purpose, we employ the spherically symmetric steady accretion flows through the standing shock wave in this paper. Following Yamasaki & Yamada (2005), we solve the time-independent hydrodynamical equations from the shock front down to the inner boundary,

$$4\pi r^2 \rho v_r = \dot{M}, \quad (20)$$

$$v_r \frac{dv_r}{dr} + \frac{1}{\rho} \frac{dP}{dr} + \frac{GM_{\text{in}}}{r^2} = 0, \quad (21)$$

$$v_r \frac{de}{dr} - \frac{P}{\rho^2} v_r \frac{d\rho}{dr} = \frac{Q_E}{\rho}, \quad (22)$$

$$v_r \frac{dY_e}{dr} = Q_N, \quad (23)$$

where \dot{M} and v_r are the mass accretion rate and radial velocity, respectively. Given the post-shock values for density, radial velocity, entropy and electron fraction ($\rho_{\text{post}}, v_{\text{post}}, s_{\text{post}}, Y_{\text{epost}}$), the shock radius is determined so that the density obtained at the inner boundary should agree with the fixed value, $\rho_{\text{in}} = 10^{11} \text{ g/cm}^3$.

The post-shock values are calculated from the corresponding pre-shock values by the Rankine-Hugoniot relations. The pre-shock values, on the other hand, are obtained from the mass accretion rate, the outer boundary conditions for entropy and electron fraction ($s_{\text{out}}, Y_{\text{eout}}$) and the assumption that matter falls freely with no interaction with neutrinos outside the shock;

$$v_{\text{pre}} = -\sqrt{2GM_{\text{in}}/R_s}, \quad (24)$$

$$\rho_{\text{pre}} = -\frac{\dot{M}}{4\pi r^2 v_{\text{pre}}}, \quad (25)$$

$$s_{\text{pre}} = s_{\text{out}}, \quad (26)$$

$$Y_{\text{epre}} = Y_{\text{eout}}, \quad (27)$$

where R_s is the shock radius. The entropy and the electron fraction at the outer boundary are assumed to be $s_{\text{out}} = 3 k_B/\text{baryon}$ and $Y_{\text{eout}} = 0.5$, respectively.

In the numerical simulations, axisymmetry but no equatorial symmetry is assumed. At the outer boundary, we adopt the fixed boundary condition consistent with the unperturbed state. On the other hand, the free-flow-in boundary condition is used at the inner boundary. A realistic tabulated EOS by Shen et al. (1998) is used both for the simulations and for the preparation of the initial conditions.

For all the models investigated in this paper, the mass accretion rate and the mass of central object are fixed to be $\dot{M} = 1 M_\odot/\text{s}$ and $M_{\text{in}} = 1.4 M_\odot$, respectively. The neutrino temperatures are also fixed to $T_{\nu_e} = 4 \text{ MeV}$ and $T_{\bar{\nu}_e} = 5 \text{ MeV}$, the typical values in the post-bounce phase. On the other hand, we systematically vary the neutrino luminosity within the range of $L_\nu = 3.0\text{--}7.0 \cdot 10^{52} \text{ erg/s}$ for different models. Note that these values are constant in time for each model. This is necessary to realize the steady unperturbed states.

To study the instability, we add angular-dependent perturbations, $\delta v_r(r, \theta)$, to the radial velocity initially;

$$v_r(r, \theta) = v_r^{1D}(r) + \delta v_r(r, \theta), \quad (28)$$

where v_r^{1D} is the spherically symmetric unperturbed velocity. The $\ell = 1$ ($\delta v_r(r, \theta) \propto \cos \theta$) single-mode perturbation and the random multi-mode perturbation are investigated. In the former case, the perturbation amplitude is set to be 1% of the unperturbed velocity. For the latter case, the amplitude is less than 1% for each radial direction. In both cases, the assumed initial amplitudes are found to be small enough to observe clearly the linear growths of the instability.

3. Results

3.1. Basic Features

The unperturbed spherically symmetric steady accretion flows are displayed in Fig. 1 for $L_\nu = 3.0, 5.5, 6.0 \cdot 10^{52} \text{ erg/s}$. As L_ν increases, the width between the shock and the neutrino sphere, $w_s = R_s - r_\nu$, becomes larger with both the neutrino sphere and the shock radius getting larger. In the cases of $L_\nu = 5.5, 6.0 \cdot 10^{52} \text{ erg/s}$, the region with a negative entropy-gradient is formed behind the shock, where the net heating rate is positive. The supernova core is convectively unstable in this region. In the case of $L_\nu = 3.0 \cdot 10^{52} \text{ erg/s}$, on the other hand, the net heating rate is always negative over the whole region from the shock down to the neutrino sphere, since the shock radius is smaller and the temperature is higher, implying more efficient coolings. As a result, there is no region with a negative entropy-gradient. Hence we can see in this case the instability solely caused by SASI. It is also noted that this model should be similar to the models considered by Blondin & Mezzacappa (2005) with only simple cooling terms taken into account.

We use the profiles in Fig. 1 as initial conditions for hydrodynamical simulations in 2D. Since they are obtained by solving Eqs. (20)–(23), a slight inconsistency is inevitably introduced by the mapping. For example, the shock is smoothed over a few computational grid points with the artificial viscosity in the simulations while the initial conditions satisfy

the Rankine-Hugoniot relation across the infinitesimal distance. As a result, transient oscillations are commonly found before they are damped away. In fact, we have done spherically symmetric computations for the unperturbed initial conditions using the same dynamical code before doing 2D simulations with perturbations. The purpose is two-fold. First, we can obtain this way "the steady states" for the dynamical code, which, as we have emphasized repeatedly, is critically important to see the linear growth of the instability. These simulations are also meant for the confirmation of the stability of the initial conditions against radial perturbations predicted by Yamasaki & Yamada (2005).

The temporal evolutions of the shock radii in the spherically symmetric simulations are shown in Fig. 2 for the three cases in Fig. 1 together with for $L_\nu = 6.5, 7.0 \cdot 10^{52}$ erg/s. The oscillations of shock radii are particularly clear in the early phase. The oscillation frequency is found to be inversely proportional to the neutrino luminosity. For the neutrino luminosity less than $7.0 \cdot 10^{52}$ erg/s, the oscillations are gradually damped and the shock approaches to the equilibrium radius, which is a bit different from the initial value. In the case of $L_\nu = 7.0 \cdot 10^{52}$ erg/s, however, the oscillation is slowly amplified and appears to be never settled to equilibrium. It is noted that this model is expected to be stable according to Yamasaki & Yamada (2005). The apparent discrepancy may be ascribed to the numerical errors inherent to the dynamical simulations as mentioned above. It should be also mentioned, however, that the large-amplitude oscillations as observed in the figure may cause instability even for linearly stable configurations. Since the main purpose of this paper is to investigate the stability for non-radial perturbations, we focus in the following only on the models with $L_\nu \leq 6.0 \cdot 10^{52}$ erg/s, in which the radial oscillations are damped within ~ 100 ms. After these transient features are sufficiently settled, we add non-radial velocity perturbations explained in the previous section to the profiles obtained this way and start 2D simulations.

Figure 3 shows in the meridian section the distributions of entropy (the left half of the panel) and density (the right half) for the models with $L_\nu = 5.5, 6.0 \cdot 10^{52}$ erg/s after 1% of the $\ell = 1$ single-mode velocity perturbation is added. For both models, we observe the growth of the perturbations. In the case of $L_\nu = 5.5 \cdot 10^{52}$ erg/s, the shock surface is deformed at first by the increasing amplitude of the non-radial mode and then begins to oscillate with a large amplitude. In the case of $L_\nu = 6.0 \cdot 10^{52}$ erg/s (right panels), on the other hand, in addition to the oscillations of the shock surface, we observe the substantial increase of the average shock radius as the time passes. In fact, after $t = 400$ ms, the shock radius continues to increase and appears to produce an explosion. Since the model is stable against radial perturbations as mentioned above, the non-radial instability and the neutrino heating therein are responsible for the explosion. We think that this is a reconfirmation of the claim that the instability, whatever the cause, behind the shock is helpful for the shock

revival.

In order to analyze further in detail the evolution of the instability, we conduct a mode analysis as follows. The deformation of the shock surface is decomposed into the spherical harmonic components;

$$R_s(\theta) = \sum_{\ell=0}^{\infty} a_{\ell} \sqrt{\frac{2\ell+1}{4\pi}} P_{\ell}(\cos\theta). \quad (29)$$

Since the system is axisymmetric, only $m = 0$ harmonics, nothing but Legendre polynomials, show up. The coefficients, a_{ℓ} , can be calculated by the orthogonality of the Legendre polynomials;

$$a_{\ell} = \frac{2\ell+1}{2} \int_{-1}^1 R_s(\theta) P_{\ell}(\cos\theta) d\cos\theta. \quad (30)$$

The position of the shock surface, $R_s(\theta)$, is estimated from the iso-entropic surface of $s = 5$ in the following analyses.

The temporal evolutions of the average shock radius are obtained from the $\ell = 0$ component in the above decomposition and $|\Delta R_s/R_{s,0}| = |(a_0 - R_{s,0})/R_{s,0}|$ are plotted in Fig. 4, where $R_{s,0}$ is the initial shock radius. As can be seen from the figure, after the shock surface oscillates for about 100 ms as in the symmetric simulations, it begins to increase. For the models with $L_{\nu} = 3.0, 5.5 \cdot 10^{52}$ erg/s, the shock surface is settled in ~ 50 ms to a quasi-steady state with a radius $\sim 10\%$ larger than the initial value, and keeps oscillating around it thereafter. In the case of $L_{\nu} = 6.0 \cdot 10^{52}$ erg/s, on the other hand, a continuous increase of the average shock radius is found, which will eventually lead to the explosion mentioned above. It is emphasized that even for the model with no negative entropy-gradient ($L_{\nu} = 3.0 \cdot 10^{52}$ erg/s), the exponential increase of the shock radius occurs during the same period. This demonstrates clearly that the instability has nothing to do with the convection at least for this model. The relative contributions of SASI and convection for other models will be discussed in the next section.

3.2. Linear and Nonlinear Growths of Instability

In this section, we discuss both the linear and nonlinear growths of the instability in greater detail. As reported in Foglizzo (2001, 2002); Blondin et al. (2003), the most remarkable feature of SASI is the dominance of the modes with $\ell = 1, 2$ in the instability. Hence we start with the analysis of the models with $\ell = 1$ single-mode velocity perturbation imposed initially.

Fig. 5 shows the temporal evolutions of the $\ell = 1$ and $\ell = 2$ modes. Although the result

for $L_\nu = 5.5 \cdot 10^{52}$ erg/s is plotted as a reference case, the qualitative feature is common to other models. As can be clearly seen, the evolution is divided into two phases. The initial phase lasting for ~ 100 ms represents the linear phase, where the amplitude of each mode grows exponentially. It is noted that even for the single-mode perturbation, the second harmonics is generated by the nonlinear coupling and grows exponentially also. In the linear phase, however, the second harmonics is always much smaller than the fundamental $\ell = 1$ mode. After ~ 100 ms, the amplitude of the fundamental mode is saturated at $\sim 10\%$ level and the nonlinear phase starts. It is found that soon after the nonlinear phase begins, the amplitude of the second harmonics becomes comparable to the fundamental mode. This corresponds to the instability found in the simulations by Blondin et al. (2003).

In order to obtain the linear growth rates for the fundamental mode ($\ell = 1$), we fit the amplitude of the mode, $a_1(t)$, with the following expression,

$$a_1(t) = A \exp(\gamma t) \sin(\omega t + \delta), \quad (31)$$

where γ and ω are the exponential growth rate and the characteristic oscillation frequency in the linear phase, respectively. The least square fitting is done for these parameters and the overall normalization, A , and the phase, δ . The dash dotted line in Fig. 5 represents the result. The obtained values of γ and ω are listed in Table 1 for the models with different L_ν .

According to Foglizzo (2001, 2002), the instability is produced by the cycle of the inward advection of the velocity and entropy fluctuations and the outward propagation of the pressure fluctuations (see also Blondin et al. (2003)). If this is correct, the characteristic oscillation frequency reflects the the cycle period,

$$\omega = 2\pi \cdot \left\{ \int_{r_\nu}^{R_s} dr \left[\frac{1}{c_s} + \frac{1}{v_r} \right] \right\}^{-1}, \quad (32)$$

where c_s is the sound velocity. The values of ω estimated this way are also given in Table 1. They are found to agree quite well with the numerical results. This is in contrast with the recent claim by Blondin & Mezzacappa (2005) that the propagation of pressure perturbations is responsible for the instability. Their simplified treatment of the cooling terms may be responsible for the difference. Our simulations indicate clearly that the time scale associated with the advection plays an important role in the instability. We can obviously find the L_ν -dependence of the oscillation frequency, ω , which can be understood as follows. As also presented in Table 1, the width between the shock and the neutrino sphere, $w_s = R_{s,\text{equil}} - r_\nu$, becomes larger as the luminosity increases. As a result, the oscillation frequency is expected to become lower since the fluctuations traverse longer distances in the cycle.

The growth rate, γ , on the other hand, has little dependence on the luminosity as shown in Table 1, As mentioned already, the instability occurs even in the case of $L_\nu =$

$3.0 \cdot 10^{52}$ erg/s, where the negative entropy-gradient is not formed and the structure is stable for convection. The interesting thing here is the fact that the linear growth rates are not so different between the models with and without a negative entropy-gradient. This suggests that SASI plays a dominant role in driving the non-radial motions even when the convection is also expected to occur. This issue will be further discussed later in this section again.

The simulations discussed so far have been done with the initial velocity perturbation including only the fundamental mode ($\ell = 1$). However, other modes with $\ell \geq 2$ also develop rapidly from ~ 50 ms. After ~ 100 ms, the amplitude of $\ell = 2$ mode becomes the same order as that of the fundamental mode, which has already been saturated by this time. This marks the beginning of the nonlinear phase. In fact, the $\ell = 2$ mode is also soon saturated. This transition from linear to nonlinear phase corresponds to the time of the rapid increase of the average shock radius shown in Fig. 4. Since the average radius is nothing but the $\ell = 0$ mode, this can be interpreted as a result of the nonlinear coupling of this mode with the fundamental mode and the ensuing saturation. As will be mentioned later, since the expansion of the shock is crucial to trigger the shock revival and eventual explosion, it is important that the neutrino luminosity is sustained for ~ 100 ms, the typical saturation time for SASI.

Next we discuss the models with the random multi-mode velocity perturbations. So far we confirmed that the $\ell = 1$ mode is indeed unstable to SASI. The models are meant to see which mode is dominant. In so doing, we also study the influence of the existence of a negative entropy-gradient. In Fig. 6, the temporal evolution of the spectrum of the spherical harmonics. The spherically symmetric component, the $\ell = 0$ mode, is omitted in the figure. The cases without and with a negative entropy-gradient are shown in the left and right panels, respectively. It is obvious that the modes with small ℓ 's, especially those with $\ell = 1, 2$, grow rapidly in the linear regime ($t \lesssim 100$ ms). This is particularly the case for the model without a negative entropy-gradient ($L_\nu = 3.0 \cdot 10^{52}$ erg/s) and the growths of the modes with $\ell > 10$ are negligibly small. With a negative entropy-gradient ($L_\nu = 5.5 \cdot 10^{52}$ erg/s), the broadening of spectra to larger ℓ modes is observed although the dominance of smaller ℓ modes can be still found. The convective instability may enhance the growth of higher harmonics in the linear phase. The similarity of the two cases suggest again that SASI is dominant over the convection even when the latter is operating.

Recently Foglizzo et al. (2005) discussed the linear stability for convection in the accretion flows in the supernova core. They found that the classical criterion for convection, that is, the negative entropy-gradient is not sufficient for the accretion flows, since the limited time is available for growth. Although the classical convection has greater linear-growth rates for modes with larger wave numbers, they claimed that there are minimum (k_{\min}) and maximum

(k_{\max}) wave numbers for unstable modes in the accretion flows, and that the growth rates are also modified. The important parameter is the ratio of the advection time through the gain region divided by the local timescale of buoyancy, χ , given in Eq. (40) in their paper. Applying their formula to our models, we obtain $\chi = 4 \dots 7$ for $L_\nu = 5.5 \dots 6.5 \cdot 10^{52}$ erg/s, with larger values for greater luminosities. Hence, the initial configurations are unstable against convection for these models, since the criterion, $\chi > 3$ is satisfied. The minimum and maximum wave numbers estimated in our models are $k_{\min} = 2 \dots 6 \cdot 10^{-8}$ cm $^{-1}$ and $k_{\max} = 1 \cdot 10^{-6}$ cm $^{-1}$, respectively. The smaller k_{\min} corresponds to larger luminosities. They roughly correspond to the minimum and maximum indices in the spherical harmonics, $\ell_{\min} = 2 \dots 4$ and $\ell_{\max} = 70 \dots 85$, respectively. The lower ℓ_{\min} and larger ℓ_{\max} are obtained for higher luminosities. These number appear to be consistent with the spectrum shown in Fig. 6 as also inferred from Fig. 5 in Foglizzo et al. (2005). Since the classical growth rate of convection is comparable to that of SASI in our models and the true growth rate of convection will be much smaller than the classical estimation, we think that SASI is a dominant driving force for the non-radial motions we observed so far.

It is also interesting to note that the modes with $\ell = 1, 2$ are dominant in the nonlinear regime, which begins after ~ 100 ms. As clearly seen in the broadening of the spectra in Fig. 6, various modes are amplified by nonlinear couplings with the dominant modes in this phase. The spectra are again broader for the model with a negative entropy-gradient. In both models, however, the dominance of the modes with $\ell = 1, 2$ is remarkable. This should correspond to the large deformations of shock wave found in the numerical simulations by Blondin et al. (2003) and Scheck et al. (2004). In order to make clear the reason for the dominance of these modes in the nonlinear regime, it will be required to study the nonlinear couplings of various modes in more detail.

3.3. Neutrino Heatings in SASI

Finally, we discuss the influence of the instability on the heating of matter by neutrinos. Figure 7 shows the distributions of the net heating rates in the meridian section for the models with $L_\nu = 5.5 \cdot 10^{52}$ erg/s (left panel) and $L_\nu = 6.0 \cdot 10^{52}$ erg/s (right panel). In both cases, the shock wave is asymmetric with respect to the equator, the characteristics for SASI. For $L_\nu = 5.5 \cdot 10^{52}$ erg/s, however, the average shock radius is only slightly larger than that in the unperturbed state. As a result, both the heating and cooling region are not much changed during the period from 100 ms to 200 ms. They are just oscillating. In the case of $L_\nu = 6.0 \cdot 10^{52}$ erg/s, on the other hand, not only the shock radius but also the heating region is getting larger as the time passes. It is further seen that the cooling region at 200 ms is

smaller than that at 100 ms. This is caused by the non-radial flows which carry down colder matter more efficiently than the spherical flows. The temperature near the inner boundary is lowered as a result. Since the cooling rates are roughly proportional to T^6 , the net cooling region is shrunk. This mechanism has been discussed in the context of convections over the years. It is applicable to SASI as it is. This broadening of the heating region and the shrink of the cooling region thrusts the shock wave outwards further, the positive feed back which eventually leads to the explosion as mentioned already.

This positive feed back cycle is confirmed by the comparison of the temporal evolution of the shock radius displayed in Fig. 4 and that of the net heating rate integrated over the volume inside the shock wave shown in Fig. 8. We can see the gradual and continuous increase of the net heating after ~ 200 ms coincides with the expansion of the shock wave. This should be compared with the case for $L_\nu = 5.5 \cdot 10^{52}$ erg/s, which does not produce any explosion. In this case, the average shock radius is settled to the value $\sim 10\%$ larger than the initial radius after ~ 150 ms while the net heating rate is fluctuated around a constant value during the same period.

Figure 9 shows the temporal evolutions of various energies integrated over the region inside the shock wave for the model with $L_\nu = 6.0 \cdot 10^{52}$ erg/s. The explosion energy shown in the figure is defined as the total energy summed only over the fluid elements which have a positive total energy and a positive radial velocity simultaneously, as was done, for example, by Yamada & Sawai (2004). It is again clearly seen that the increase of the internal energy after ~ 200 ms is responsible for the shock revival. Note that the explosion energy remains zero for a while after the shock wave begins its continuous expansion, implying that there is still no fluid element with a positive total energy and radial velocity at that time, and that it is only after another ~ 100 ms that some of the fluid elements gain enough energy to be ejected.

4. Conclusion

We have done two-dimensional simulations of SASI in the supernova core to study its linear growth and nonlinear saturation in detail together with its role in the shock revival. We employed the realistic EOS and neutrino interaction rates for emission and absorption on nucleons. The systematic numerical experiments have been conducted, varying neutrino luminosities from the central object and solving spherically symmetric steady accretion flows through the stalled shock wave as unperturbed initial conditions. We have studied the models both with and without a negative entropy-gradient in the initial configurations. We have done the mode analysis based on the spherical harmonics decomposition. Not only the $\ell = 1$

single-mode velocity perturbation with an amplitude of 1% but also the random multi-mode velocity perturbation with an amplitude $< 1\%$ everywhere has been investigated.

We have demonstrated that the non-radial instability grows, indeed, exponentially in all the models. In a model with a relatively high neutrino luminosity, we have found a continuous expansion of the shock wave, which will eventually lead to explosion. Since this model did not produce explosion in the spherically symmetric simulations, we can infer that the instability tends to lower the critical neutrino luminosity for the shock revival.

In the mode analysis for the models with the initial $\ell = 1$ single-mode velocity perturbation, we have clearly seen both the linear and nonlinear growths of the instability. We have obtained the growth rates and characteristic oscillation frequencies by fitting the numerical data and found that the oscillation frequency reflects the period of the cycle of the inward advectations of the velocity- and entropy-fluctuations and the outward propagations of pressure fluctuations. This fact suggests that the instability is indeed driven by such cycles. This is, however, in sharp contrast with the recent findings by Blondin & Mezzacappa (2005) that the repeated propagations of pressure fluctuations are solely responsible for the instability. This apparent discrepancy may be ascribed to the difference of the treatments of neutrino cooling.

We have observed for the models with the random multi-mode velocity fluctuation that the linear phase lasts for ~ 100 ms, in which the modes with $\ell = 1, 2$ are dominant. It is also interesting that in the nonlinear phase, where the nonlinear couplings generate all modes and the saturation occurs, the modes with $\ell = 1, 2$ are still dominant. Detailed analyses of the mode couplings will be necessary to reveal the physics behind this result. In the models with a negative entropy-gradient, the broadening of the spectra has been observed, which we have ascribed to the convective motions. This appears to be supported by the recent analysis of the convection in the accretion flows in a supernova core by Foglizzo et al. (2005). Applying their results to our models, we have shown that the convection plays a minor role in our models. The relative significance of SASI and convection, however, depends on the situations and SASI appears to be dominant for relatively low neutrino luminosities (Scheck et al. 2004). It is important to note here that the growth of SASI is rather slow and takes ~ 100 ms. Although we have found a shock revival due to the SASI-enhanced neutrino heatings in some cases as mentioned above, whether we find such a revival in the reality crucially depends on if the neutrino luminosity can be sustained for this period, not an easy job.

If SASI alone cannot get the job done, we will have to find something more to boost the shock revival. We are currently working on some combinations of microphysics and SASI and will soon publish the results elsewhere (Ohnishi et al. 2005). The influence of rotation

on SASI should be addressed also and may be important for the possible correlation of the kick velocity and the rotation axis (Wang et al. 2005; Ohnishi et al. 2005).

We are grateful to K. Sumiyoshi for valuable discussions and for providing us with the tabulated equation of state, which can be handled without difficulties. We also thank T. Yamasaki and M. Watanabe for providing us with the information about their models. K.K. expresses thanks to K. Sato for continuing encouragements. The numerical calculations were partially done on the supercomputers in RIKEN and KEK (KEK supercomputer Projects No.02-87 and No.03-92). This work was supported in part by the Japan Society for Promotion of Science(JSPS) Research Fellowships (K.K.), Grants-in-Aid for the Scientific Research from the Ministry of Education, Science and Culture of Japan (No.S14102004, No.14079202, No.17540267), and Grant-in-Aid for the 21st century COE program “Holistic Research and Education Center for Physics of Self-organizing Systems”.

REFERENCES

- Akiyama, S., Wheeler, J. C., Meier, D. L., & Lichtenstadt, I. 2003, *ApJ*, 584, 954
- Ardeljan, N. V., Bisnovatyi-Kogan, G. S., & Moiseenko, S. G. 2000, *A&A*, 355, 1181
- Blondin, J. M., Mezzacappa, A., & DeMarino, C. 2003, *ApJ*, 584, 971
- Blondin, J. M., & Mezzacappa, A. 2005, submitted to *ApJ*, astro-ph/0507181
- Bruenn, S. W. 1985, *ApJS*, 58, 771
- Burrows, A., Hayes, J., & Fryxell, B. A. 1995, *ApJ*, 450, 830
- Burrows, A. & Hayes, J. 1996, *Physical Review Letters*, 76, 352
- Foglizzo, T. 2001, *A&A*, 368, 311
- Foglizzo, T. 2002, *A&A*, 392, 353
- Foglizzo, T., Scheck, L., & Janka, H.-T. 2005, astro-ph/0507636
- Fryer, C. L. 2004, *ApJ*, 601, L175
- Houck, J. C., & Chevalier, R. A. 1992, *ApJ*, 395, 592
- Herant, M., Benz, W., Hix, W. R., Fryer, C. L., & Colgate, S. A. 1994, *ApJ*, 435, 339

- Janka, H.-T., & Mueller, E. 1996, *A&A*, 306, 167
- Janka, H.-T., Kifonidis, K., & Rampp, M, 2001, in *Physics of Neutron Star Interiors*, edited by D. Blaschke, N.K. Gledenning, and A. Sedrakian (Springer-Verlag, Berlin), 568 of Lecture Notes in Physics (astro-ph/0103015)
- Khokhlov, A. M., Höflich, P. A., Oran, E. S., Wheeler, J. C., Wang, L., & Chtchelkanova, A. Y. 1999, *ApJ*, 524, L107
- Kotake, K., Yamada, S., & Sato, K. 2003, *ApJ*, 595, 304
- Kotake, K., Sawai, H., Yamada, S., & Sato, K. 2004, *ApJ*, 608, 391
- Kotake, K., Yamada, S., & Sato, K. 2005, *ApJ*, 618, 474
- Kotake, K., Sato, K., & Takahashi, K. 2005, submitted to *Reports on Progress in Physics*, astro-ph/0509456
- Leonard, D. C., Filippenko, A. V., Ardila, D. R., & Brotherton, M. S. 2001, *ApJ*, 553, 861
- Mönchmeyer, R, M., & Müller, E. 1989, in *NATO ASI Series, Timing Neutron Stars*, ed. H. Ögelman & E.P.J van der Heuvel (New York: ASI)
- Müller, E., Rampp, M., Buras, R., Janka, H.-T., & Shoemaker, D. H. 2004, *ApJ*, 603, 221
- Ohnishi, N., Kotake, K., & Yamada, S. 2005 in preparation
- Rampp, M., & Janka, H.-T. 2002, *A&A*, 396, 361
- Shimizu, T. M., Ebisuzaki, T., Sato, K., & Yamada, S. 2001, *ApJ*, 552, 756
- Scheck, L., Plewa, T., Janka, H.-T., Kifonidis, K., Müller, E. 2004, *Physical Review Letters*, 92, 011103
- Shen, H., Toki, H., Oyamatsu, K., Sumiyoshi, K. 1998, *Nuclear Physics*, A637, 43, 109, 301
- Stone, J. M. & Norman, M. L. 1992, *ApJS*, 80, 753
- Walder, R., Burrows, A., Ott, C. D., Livne, E., Lichtenstadt, I., & Jarrar, M. 2005, *ApJ*, 626, 317
- Wang, L., Wheeler, J. C., Li, Z., & Clocchiatti, A. 1996, *ApJ*, 467, 435
- Wang, L., Howell, D. A., Höflich, P., & Wheeler, J. C. 2001, *ApJ*, 550, 1030

Wang, L., et al. 2002, ApJ, 579, 671

Wang, C., Lai, D., and Han, J. 2005 submitted to ApJ, astro-ph/0509484

Wheeler, J. C., Yi, I., Höflich, P., & Wang, L. 2000, ApJ, 537, 810

Yamada, S. & Sato, K. 1994, ApJ, 434, 268

Yamada, S. & Sawai, H. 2004, ApJ, 608, 907

Yamasaki, T., & Yamada, S. 2005, ApJ, 623, 1000

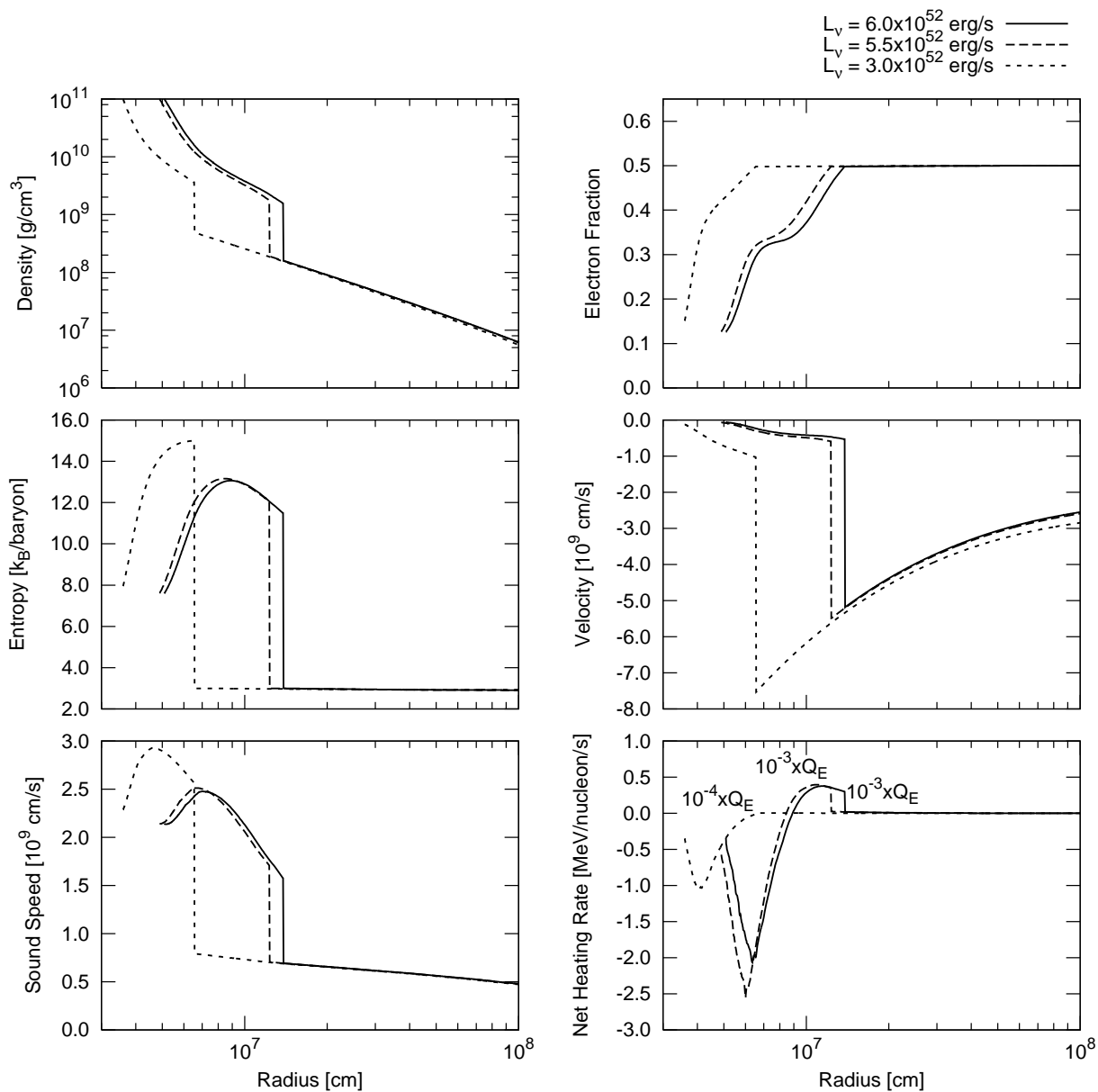


Fig. 1.— Physical quantities in unperturbed spherically symmetric accretion flows. Solid, dashed, and dotted lines represent the solutions for $L_\nu = 6.0 \cdot 10^{52}$, $5.5 \cdot 10^{52}$, and $3.0 \cdot 10^{52}$ erg/s, respectively.

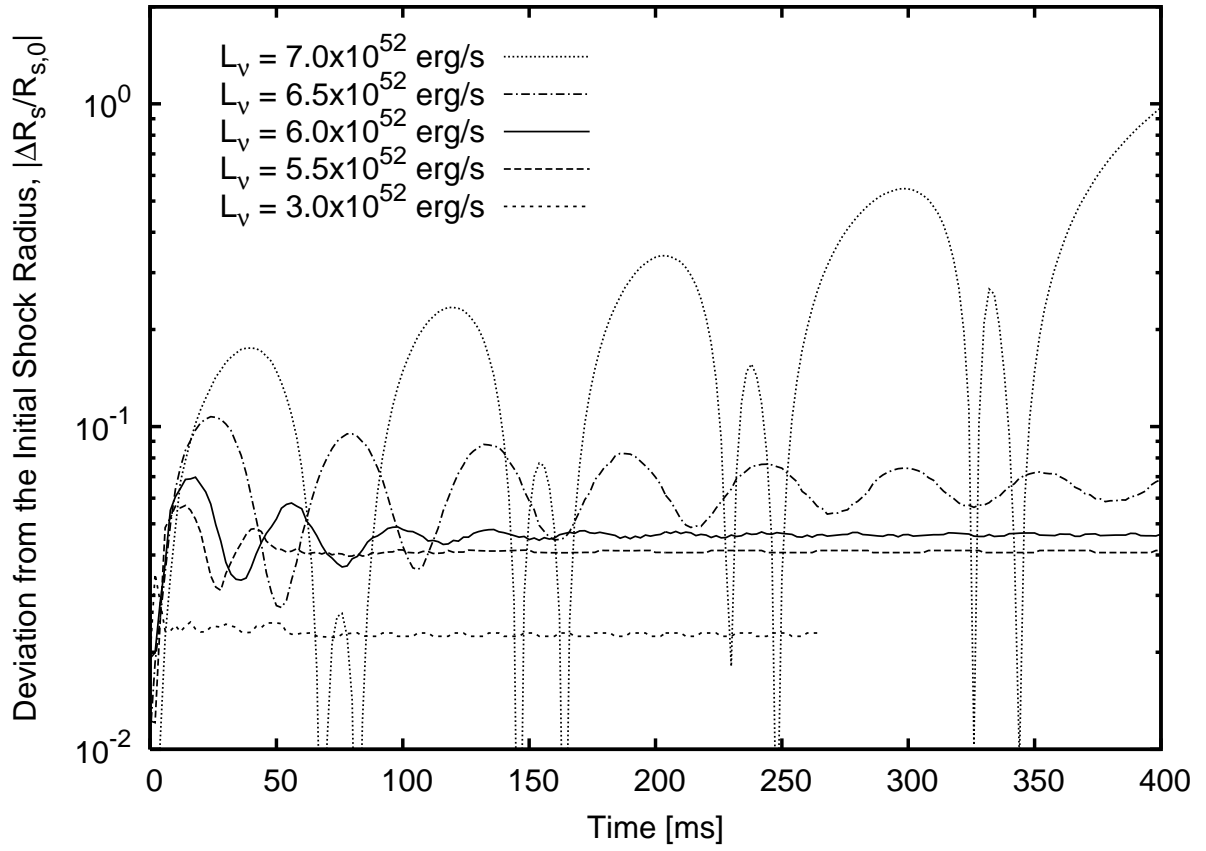


Fig. 2.— Temporal evolutions of shock radius in the spherically symmetric simulations for the models given in Fig. 1 together with for $L_\nu = 6.5, 7.0 \cdot 10^{52}$ erg/s. The relative deviation from the initial value is plotted

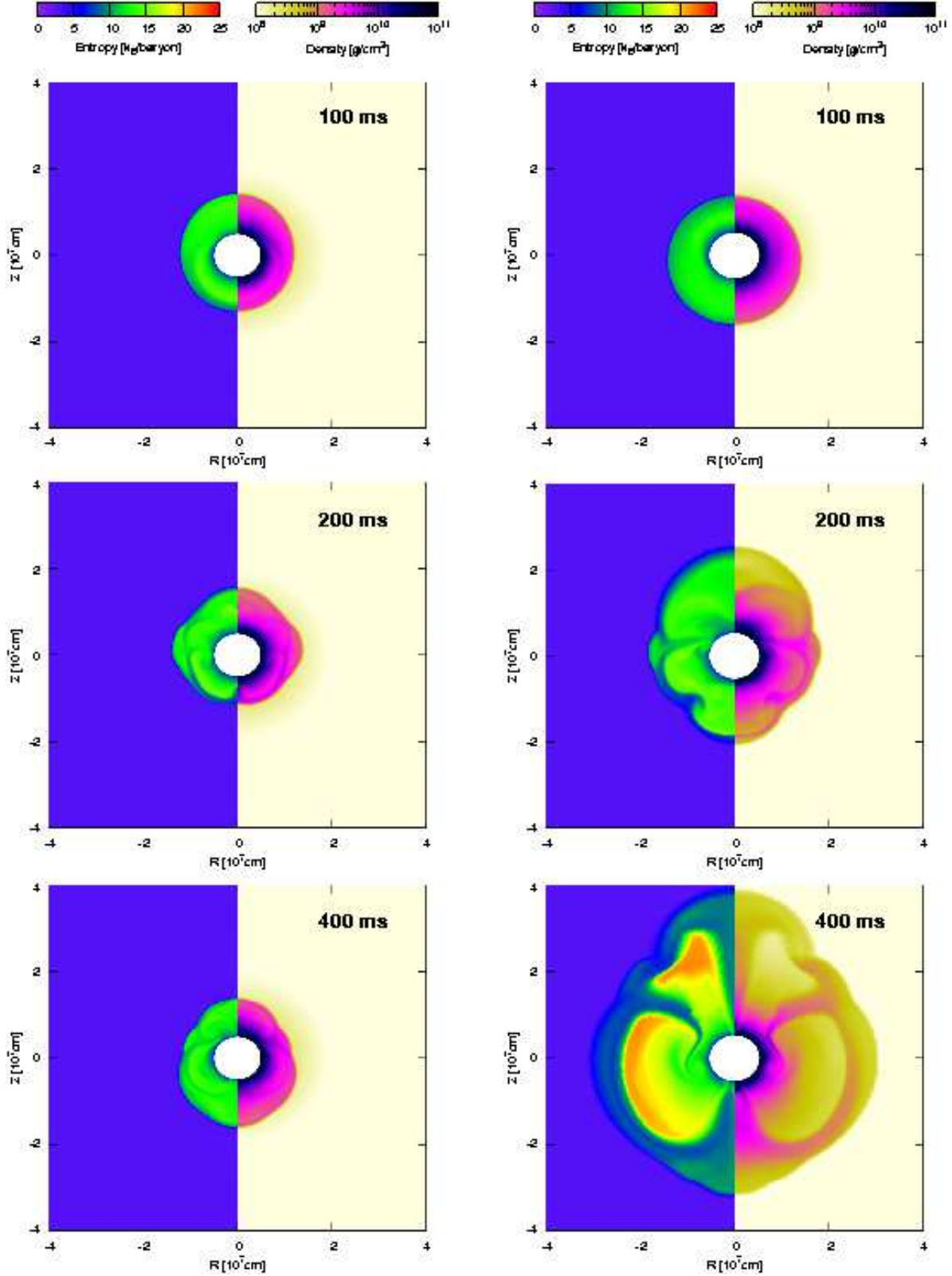


Fig. 3.— Entropy- (the left half of each panel) and density- (the right half) distributions in the meridial section for 1% of the $\ell = 1$ single-mode velocity perturbation. $L_\nu = 5.5 \cdot 10^{52}$ erg/s is assumed for the left panels and $L_\nu = 6.0 \cdot 10^{52}$ erg/s is for the right panels.

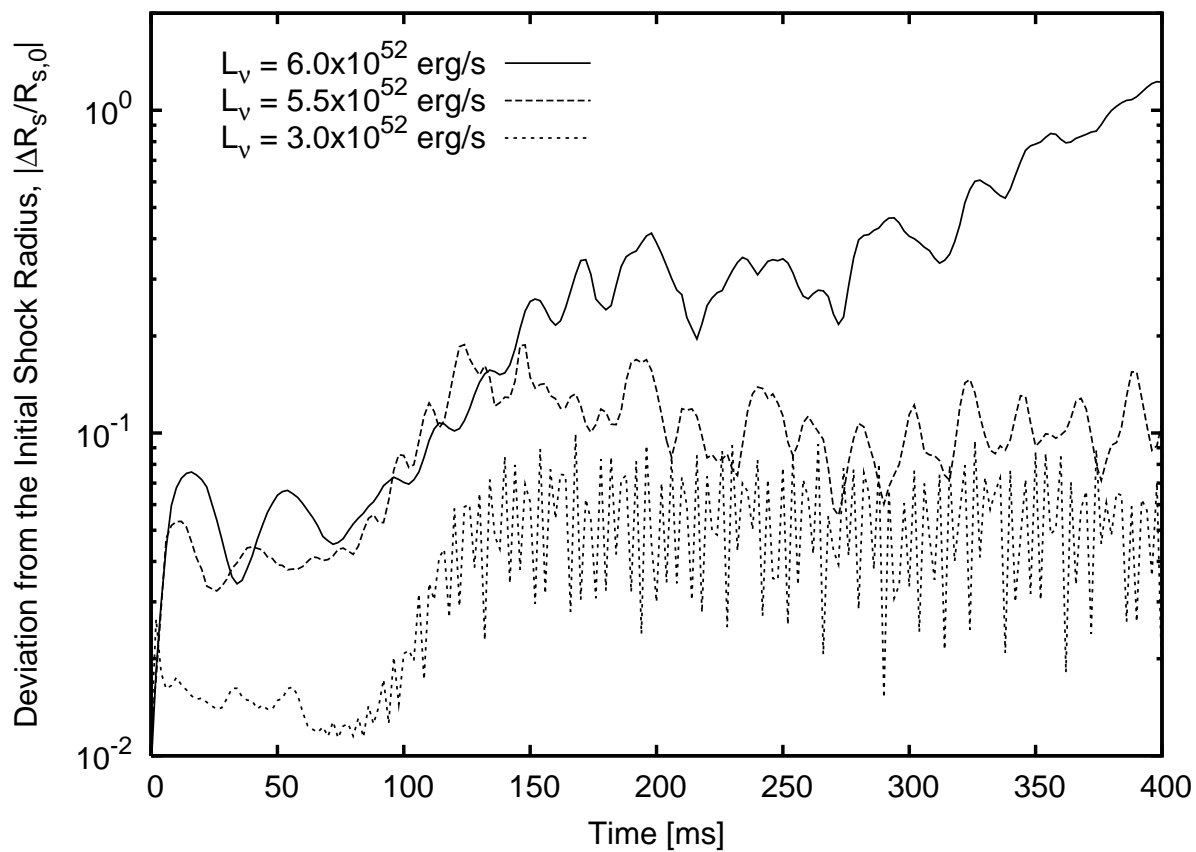


Fig. 4.— Temporal evolutions of the $\ell = 0$ component in the spherical harmonic decompositions. The relative deviation from the initial value is plotted.

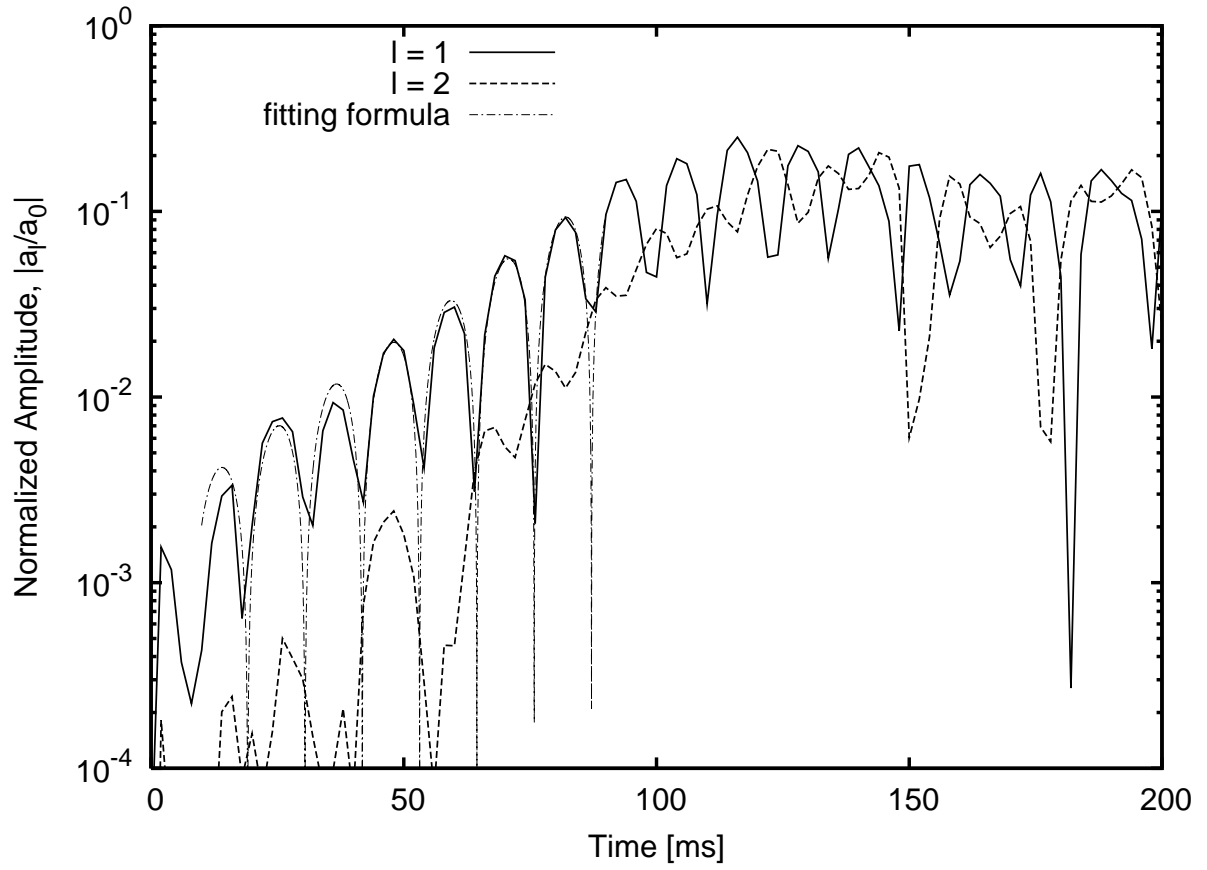


Fig. 5.— Temporal evolutions of the normalized amplitudes of the $\ell = 1, 2$ modes for the model with $L_\nu = 5.5 \cdot 10^{52}$ erg/s. The dot-dashed line represents the fitting in the linear phase.

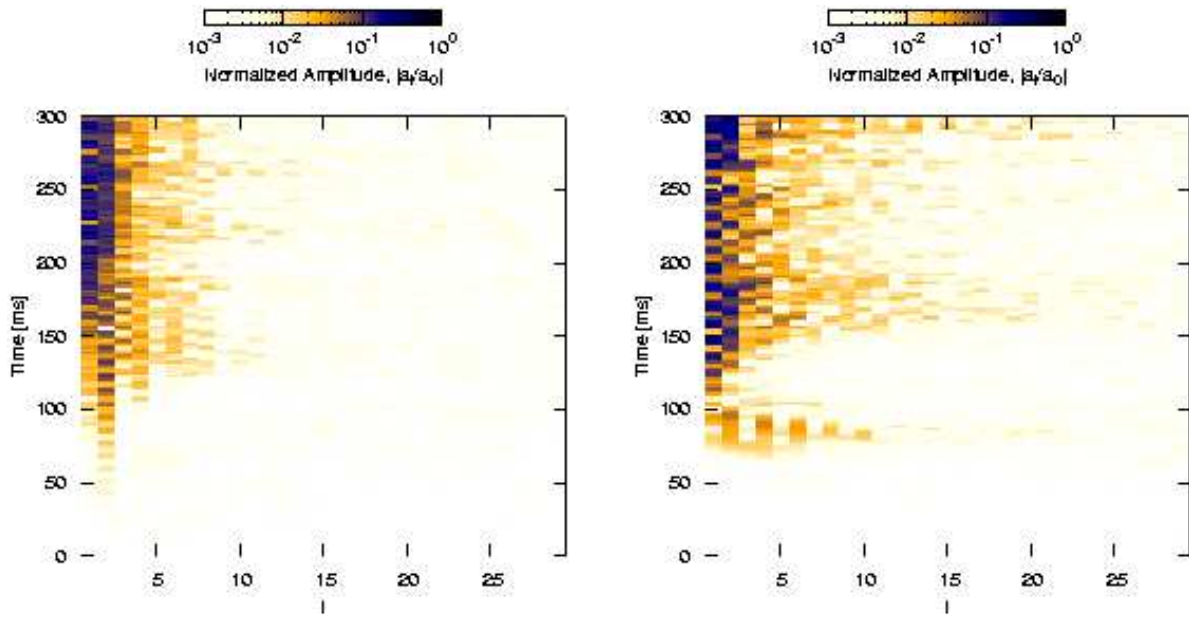


Fig. 6.— Temporal evolutions of the spectra in the spherical harmonics decomposition for the models with $L_\nu = 3.0 \cdot 10^{52}$ erg/s (left panel) and with $L_\nu = 5.5 \cdot 10^{52}$ erg/s (right panel). The random multi-mode velocity perturbations are initially added.

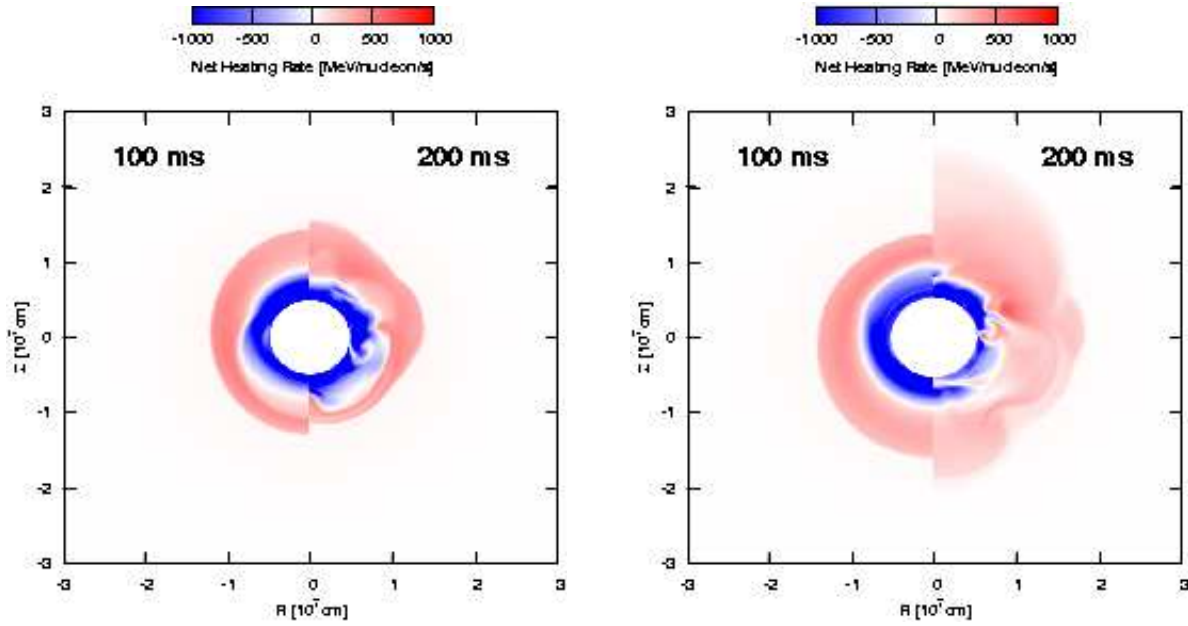


Fig. 7.— Net heating rates in the meridian section for the models with $L_\nu = 5.5 \cdot 10^{52}$ erg/s (left panel) and $L_\nu = 6.0 \cdot 10^{52}$ erg/s (right panel). 1% of the $\ell = 1$ single-mode velocity perturbation is initially added. The left (right) half of each panel represents the result for 100 (200) ms.

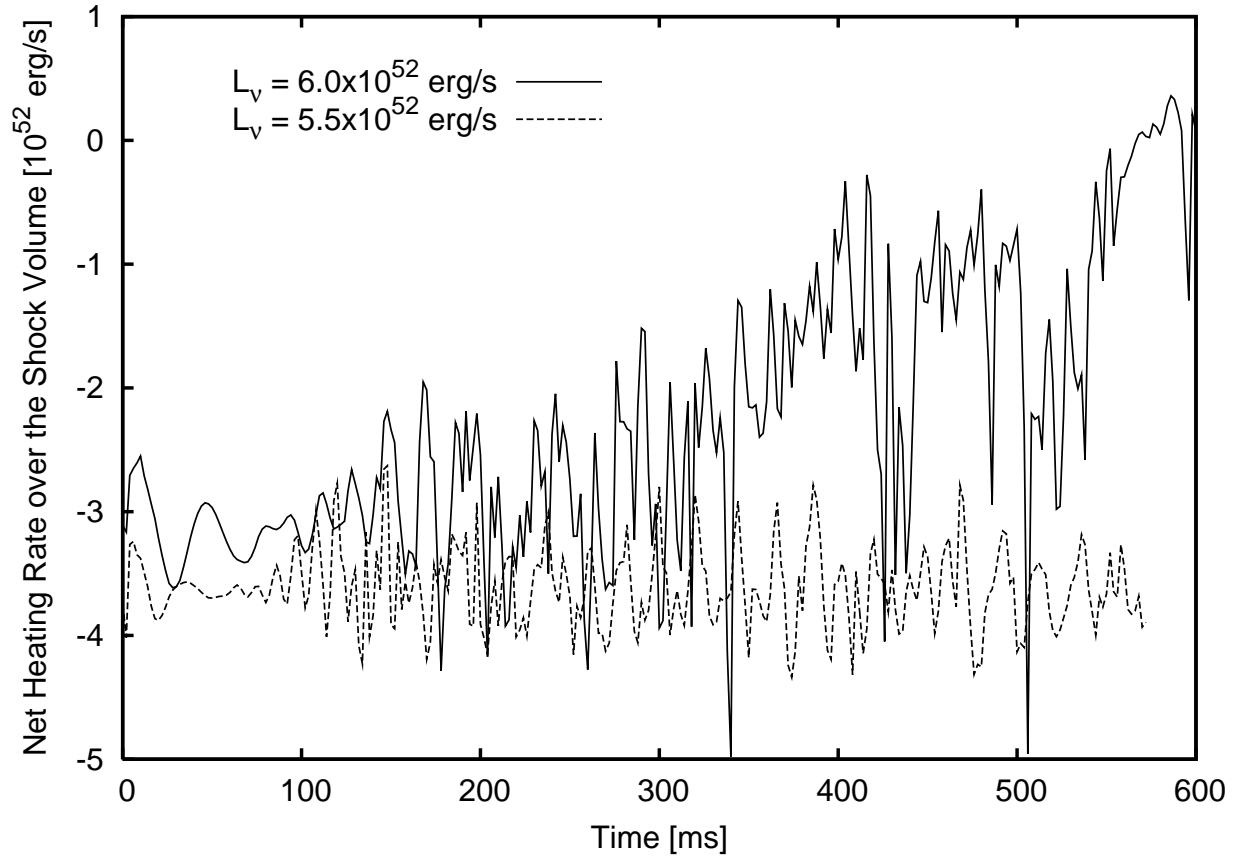


Fig. 8.— Temporal evolutions of the net heating rate integrated over the region inside the shock wave. The solid and dashed lines represent the models with $L_\nu = 6.0 \cdot 10^{52}$ erg/s and $L_\nu = 5.5 \cdot 10^{52}$ erg/s, respectively. 1% of the $\ell = 1$ single-mode velocity perturbation is initially added.

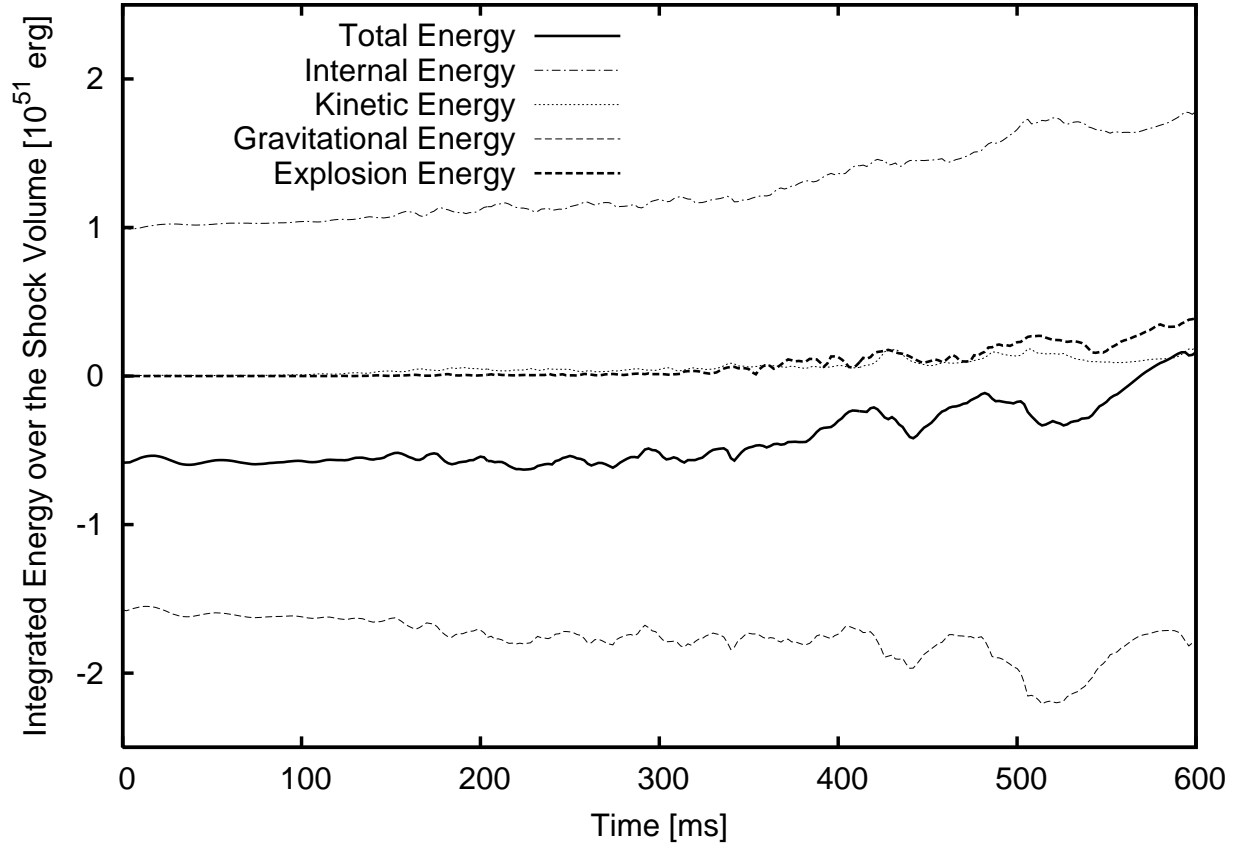


Fig. 9.— Temporal evolutions of various energies integrated over the region inside the shock wave for the model with $L_\nu = 6.0 \cdot 10^{52}$ erg/s. 1% of the $\ell = 1$ single-mode velocity perturbation is initially added. See the text for the definition of the explosion energy.

Table 1. Key Variables in SASI.

L_ν (10^{52} erg/s)	γ (s^{-1})	ω (s^{-1})	$R_{s,\text{equil}}$ (10^5 cm)	w_s (10^5 cm)	ω_{adv} (s^{-1})	ω_{snd} (s^{-1})	ω_{cyc} (s^{-1})
3.0	42.4	915	66.9	30.9	1098	5867	925
5.5	45.7	277	128	79.2	262	1832	229
6.0	38.3	188	144	93.5	207	1497	181
6.5	35.6	143	167	114	159	1199	141

Note. — L_ν represents the model luminosities. The growth rate and the oscillation frequency denoted as γ and ω , respectively, are obtained by the least square fitting to the numerical results in the linear regime. $R_{s,\text{equil}}$ is the initial shock radius and w_s is the distance between the shock radius and the neutrino sphere; $w_s = R_{s,\text{equil}} - r_\nu$. The frequencies associated with the advection and the sound-propagation between the shock and the neutrino sphere are denoted as ω_{adv} and ω_{snd} , respectively, and are defined as $\omega_{\text{adv}} = 2\pi / \int_{r_\nu}^{R_s} (1/v_r) dr$ and $\omega_{\text{snd}} = 2\pi / \int_{r_\nu}^{R_s} (1/c_s) dr$, respectively. They are evaluated numerically for the initial conditions. The characteristic frequency of SASI is given by the cycle frequency, $\omega_{\text{cyc}} = 2\pi / [\int_{r_\nu}^{R_s} (1/v_r) dr + \int_{r_\nu}^{R_s} (1/c_s) dr]$. See the text for more detail.